LASER & PHOTONICS REVIEWS
www.lpr-journal.org

High Performance 1.3 µm III–V Quantum Dot Lasers Grown on Silicon via all MOCVD Epitaxy

Honghwi Park, Seungchul Lee, Won Seok Han, Daehwan Jung, and HoSung Kim**

Epitaxial growth of III-V light sources onto silicon (Si) platforms is technologically important for numerous applications in photonics. High-performance quantum dot (QD) lasers on Si have been carried out using molecular beam epitaxy systems because they can permit precise epitaxy control for sophisticated III–V QD growth and low epitaxy temperatures. Although the metal-organic chemical vapor deposition system (MOCVD) is the choice of the III–V optoelectronics industry and more advantageous for Si photonic platform integrations, no high-performance, reliable III–V lasers epitaxially integrated onto Si have been demonstrated using MOCVD. Here, all-MOCVD-grown III–V QD lasers on Si with a threshold current density of 255 A cm^{-2} are shown, lasing up to 115 °C, and extrapolated device lifetimes exceeding 20 years when aged at 55 °C. These impressive results are achieved by solving two critical issues, which are the growth of high-quality QDs and two-step *p*-$Al_{0.4}Ga_{0.6}As$ cladding growth without free carrier absorption. This work paves the way for commercializing Si photonics integrated with efficient and reliable III-V on-chip light sources in a scalable fashion.

1. Introduction

Silicon (Si) photonics is a crucial technology for various applications, including integrated optical interconnects[1,2] and high-speed datacom/telecoms.[3] Integrating efficient and reliable III–V light sources onto Si is more appealing for compact and scalable photonics platforms than relying on external laser diodes.[4,5] However, achieving this has remained the holy grail in the research community for many decades.[6] While the wafer bonding approach has been commercialized,[7] direct epitaxy of III–V materials still has advantages such as higher scaling, simpler device processing, and lower fabrication cost.[8–10] Epitaxially grown III–V quantum dot (QD) lasers emitting at the 1.3 µm communication wavelength have shown great performances in low threshold current density,[9,11] high temperature lasing,[12] low reflection sensitivity,[13] and highly improved device lifetimes,[9,14] thanks to their strong carrier confinements in all dimensions and the advances in the III–V buffer growth on Si.[15] However, all the previous high-performance QD lasers on Si were grown by molecular beam epitaxy (MBE) reactors[10,11] because MBE growth offers precise epitaxy control required for the sophisticated III–V QD growths.

Metal-organic chemical vapor deposition (MOCVD) is the choice of epitaxial tool in the optoelectronics industry with its larger growth throughput. A recent report on GaAs nano-ridge laser diodes fabricated on a 300-mm Si wafer using MOCVD confirms that this approach is a highly capable method for achieving monolithic integration of laser diodes on a Si photonics platform.[5] Furthermore, selective area growth offered by MOCVD is another key advantage over MBE for integrating on-chip light sources onto Si photonic platforms,[8,10,16,17] since III-V materials may

H. Park, S. Lee, W. S. Han, H. Kim
Photonic/Wireless Devices Research Division
Electronics and Telecommunications Research Institute (ETRI)
Daejeon 34129, Republic of Korea

H. Park
School of Electronic Engineering
Kumoh National Institute of Technology
Gumi-si, Gyeongbuk 39177, Republic of Korea

S. Lee
Department of Materials Science and Engineering
Korea Advanced Institute of Science and Technology (KAIST)
Daejeon 34141, Republic of Korea

D. Jung
Center for Quantum Technology
Korea Institute of Science and Technology (KIST)
Seoul 02792, Republic of Korea
E-mail: daehwan.jung@kist.re.kr

D. Jung
Nanoscience and Technology
KIST School at University of Science and Technology
Seoul 02792, Republic of Korea

H. Kim
Samsung Advanced Institute of Technology (SAIT) Device Research Center
Samsung Electronics, Co. Ltd.
130 Samsung-ro, Yeongtong-gu, Suwon-si, Gyeonggi-do 16678, Republic of Korea
E-mail: h2o2.kim@samsung.com

The ORCID identification number(s) for the author(s) of this article can be found under https://doi.org/10.1002/lpor.202500574

DOI: 10.1002/lpor.202500574

need to be selectively grown on exposed crystalline surface for Si waveguide light coupling.[10,18–20] The low optical coupling efficiencies reported from the recent MBE-grown III–V Si lasers arise from the large air gap between the III–V active region facet and the Si waveguide,[18,19] which is physically inevitable for MBE growth. There have been tremendous efforts to grow high-quality InAs/GaAs QDs emitting at the technologically important 1310 nm wavelength using MOCVD for laser applications, but those III–V QD lasers have completely failed to match the performance of the MBE counterparts for two reasons. The first is the poor quality of MOCVD-grown III–V QDs and the second is the high growth temperature for *p*-type AlGaAs cladding after the QD active region. Especially, the latter is critical because a typical *p*-$Al_{0.4}Ga_{0.6}As$ upper cladding layer is grown at 700 °C or higher in an MOCVD reactor, which results in serious thermal degradation of InAs QDs.[21,22] Lower temperature growths, however, lead to a poor crystalline quality with catastrophic free carrier absorption in the laser epi-structure. To avoid this issue, recent studies employed a *p*-InGaP cladding grown at 500 °C, but they also showed highly compromised QD laser performances with limited continuous-wave (CW) operation temperatures and escalated threshold current densities.[23]

In this work, we demonstrate high performance and reliable InAs/GaAs QD lasers grown on on-axis (001) Si substrates using all-MOCVD epitaxy. We achieve unparalleled QD laser performances in terms of low threshold current density (255 A cm^{-2}) and CW operation temperature up to 100 °C (115 °C in pulsed mode) by growing high-quality QDs and a two-step *p*-AlGaAs clad structure. In particular, the latter approach effectively prevents thermal degradation and free carrier absorption in the QD active region. Furthermore, high-quality GaAs buffer layers on Si with a threading dislocation density (TDD) of 9×10^6 cm^{-2} allow excellent device reliability with extrapolated lifetimes exceeding 20 years when aged at 55 °C. We believe that this work is a major step toward monolithically integrating III-V light sources onto Si photonic platforms using a scalable epitaxial approach.

2. Results

2.1. Growth of High-Quality InAs/GaAs QDLDs on Si (100)

Figure 1 shows the material characteristics of all-MOCVD-grown InAs/GaAs QD laser diode (QDLD) heterostructures on Si (100) substrate using a MOCVD system. Figure 1a,b depict a schematic and a cross-section transmission electron microscope (TEM) image of the InAs/GaAs QDLD heterostructures directly grown on the GaP/Si (100) template, respectively. The full QDLD structure consists of a 2.5 μm-thick GaAs buffer and an edge-emitting LD structure with seven-pair QD-in-a-well (DWELL) layers. The TEM image reveals the low-defect GaAs buffer with high-quality QDs as we designed. In the seven pairs of DWELL active layers, which can be seen in Figure 1c, no defects were observed around the QDs. Additionally, clear satellite fringes were observed from high-resolution X-ray diffraction measurements (see Figure S1 in Supporting Information), which suggests coherent growth of the DWELL active layers. Furthermore, the evidence of threading dislocation annihilation process can be observed in the GaAs buffer region, including three pairs of dislocation filter layers (DFLs) as depicted in Figure 1d, merging with the misfit dislocations.

To clarify the quality of GaAs buffer quantitatively, a TDD on the surface of the GaAs buffer on Si was measured by electron channeling contrast imaging (ECCI) as depicted in Figure 1e. The TDD values of the GaAs buffer on Si without DFLs and with DFLs were 1×10^8 and 9×10^6 cm^{-2}, respectively. The TDD level between them differs by more than one order of magnitude, highlighting the significant impact of the embedded DFLs. The detrimental effect of threading dislocations, which damages the QDs, is clearly observed in the cross-section TEM image of the QDs grown on Si without DFLs (Figure 1f). A 200 nm-thick InGaAs single layer was also studied as a dislocation filter layer, but it was not effective in our MOCVD-grown GaAs buffers. Figure 1g shows an atomic-force microscope (AFM) image of QDs on a Si substrate with DFLs, indicating a QD density of 6.2×10^{10} cm^{-2} and uniform distribution of QDs. Comparing the TDD and QD density at the same scale as indicated by the black square in Figure 1e reveals that the estimated number of damaged QDs on Si with DFLs can be ignorable due to the low TDD level. As a result of the effect of threading dislocations on the QDs, the photoluminescence (PL) characteristics exhibit a significant difference, as shown in Figure 1h. While the PL center wavelength of the QD samples is almost the same, the PL intensity from the QD grown on Si with DFLs is 3.5 times higher than that without DFLs. Most importantly, the PL spectra of QDs on a GaAs substrate and Si with DFLs show nearly identical intensities. The full-width at half-maximum of the PL spectrum is 74 meV, which is higher than that of MBE-grown QDs. We believe that this can be improved by developing effective QD flushing techniques previously applied by MBE growth. Figure 1i shows a PL mapping of the QDLDs grown on a 2-inch Si wafer. The deviation of the PL center wavelength across the wafer is merely 3.78 nm, showing an excellent uniformity of the QDLD growth via MOCVD.

2.2. Low-Temperature Growth of *p*-AlGaAs Cladding Layer

Figure 2 shows the importance of the two-step *p*-AlGaAs clad structure and its impact on the optical and electrical properties. As mentioned above, all-MOCVD-grown InAs/GaAs QDLDs on Si substrate with a low-temperature *p*-InGaP cladding layer were studied previously to avoid thermal degradation of QDs.[23] However, this *p*-InGaP layer can induce several issues such as ordering and phase separation[24,25]; hence, the low-temperature growth of *p*-AlGaAs cladding layers with a controlled doping concentration is crucial for high-performance QDLDs. Figure 2a describes the effect of the free-carrier absorption, showing the PL spectra from the QDLD epi-structure with 1×10^{19} cm^{-3} doped *p*-AlGaAs cladding layer depending on the etching thickness. For the fully etched sample, the *p*-cladding etching was stopped right before the QD active layers. The result shows that the PL intensity increased as the etching thickness increased, because the free carrier absorption in *p*-AlGaAs layer was reduced.

To find an optimal doping concentration with the minimum free carrier absorption, the QDLDs with various doping concentrations in *p*-AlGaAs cladding layer were also evaluated by PL measurements as described in Figure 2b. It is found that the PL intensity was reduced as the doping concentration in *p*-AlGaAs was increased. Moreover, the PL spectra of the QDLD, having a doping concentration of 5×10^{17} cm^{-3}, show almost the same

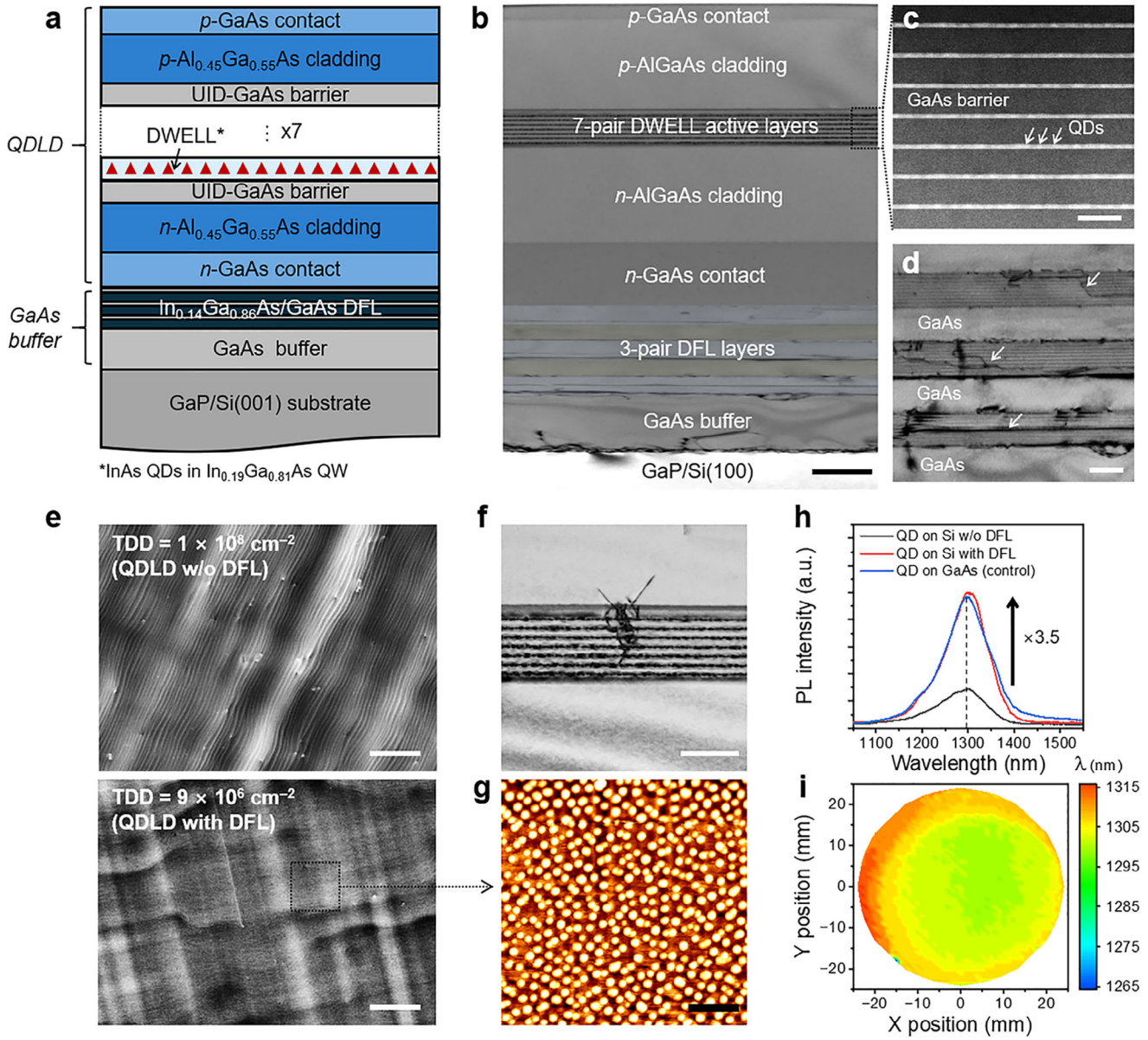

Figure 1. Material characterizations of all-MOCVD-grown InAs/GaAs QDLDs on Si (100) substrate. a) A schematic structure of the InAs/GaAs QDLDs on an on-axis Si (100) substrate. The full LD heterostructure is composed of GaAs buffer section and QDLD section. b) A cross-section TEM image of the InAs/GaAs QDLDs grown on a Si (100) substrate. Scale bar is 1 μm. c) A cross-section scanning TEM image of 7-pair DWELL active layers. QDs were clearly observed within the DWELL layer. Scale bar is 100 nm. d) A cross-section TEM image of 3-pair DFLs. Each DFL with a superlattice structure consists of 10 sets of 10 nm InGaAs layer and 10 nm GaAs layer. Scale bar is 300 nm. e) ECCI images of the GaAs buffer for evaluating TDD level between the samples without and with DFLs. The top ECCI image is the result of the GaAs buffer without DFLs, and the bottom ECCI image is the GaAs buffer with DFLs. TDD value of the GaAs buffer on Si without and with DFLs is 1×10^8 cm^{-3} and 9×10^6 cm^{-3}, respectively. Scale bar is 2 μm. f) Cross-section TEM image of DWELL on Si without DFLs. QDs were damaged by threading dislocations. Scale bar is 500 nm. g) AFM image of QDs on Si with DFLs, indicating a QD density of 6.2×10^{10} cm^{-2}. Scale bar is 500 nm. h) PL spectra of QDs on Si substrate without/with DFLs and on native GaAs substrate (for control). PL intensity of QDs on Si substrate with DFLs shows a very slight difference compared to that of QDs on GaAs substrate. i) PL mapping results of QDs grown on a two-inch Si substrate. Deviation of PL center wavelength shows 3.78 nm, showing good uniformity.

intensity as that of the pristine QDLD without a *p*-cladding layer. This indicates that the sample with a 5×10^{17} cm^{-3} doping concentration has a negligible free carrier absorption.

From these results, we further investigated the optimal growth condition of *p*-AlGaAs grown at low temperatures with a 5×10^{17} cm^{-3} doping concentration. At a low temperature ≈550 °C, AlGaAs layers are unintentionally *p*-doped due to the carbon (C)-containing aluminum (Al)-organic source, but its doping concentration is difficult to precisely control. On the other hand, zinc (Zn) atom doping, widely used as a *p*-type dopants, can induce Zn diffusion into the active medium in the subsequent high-temperature annealing process.[26] To circumvent this issue,

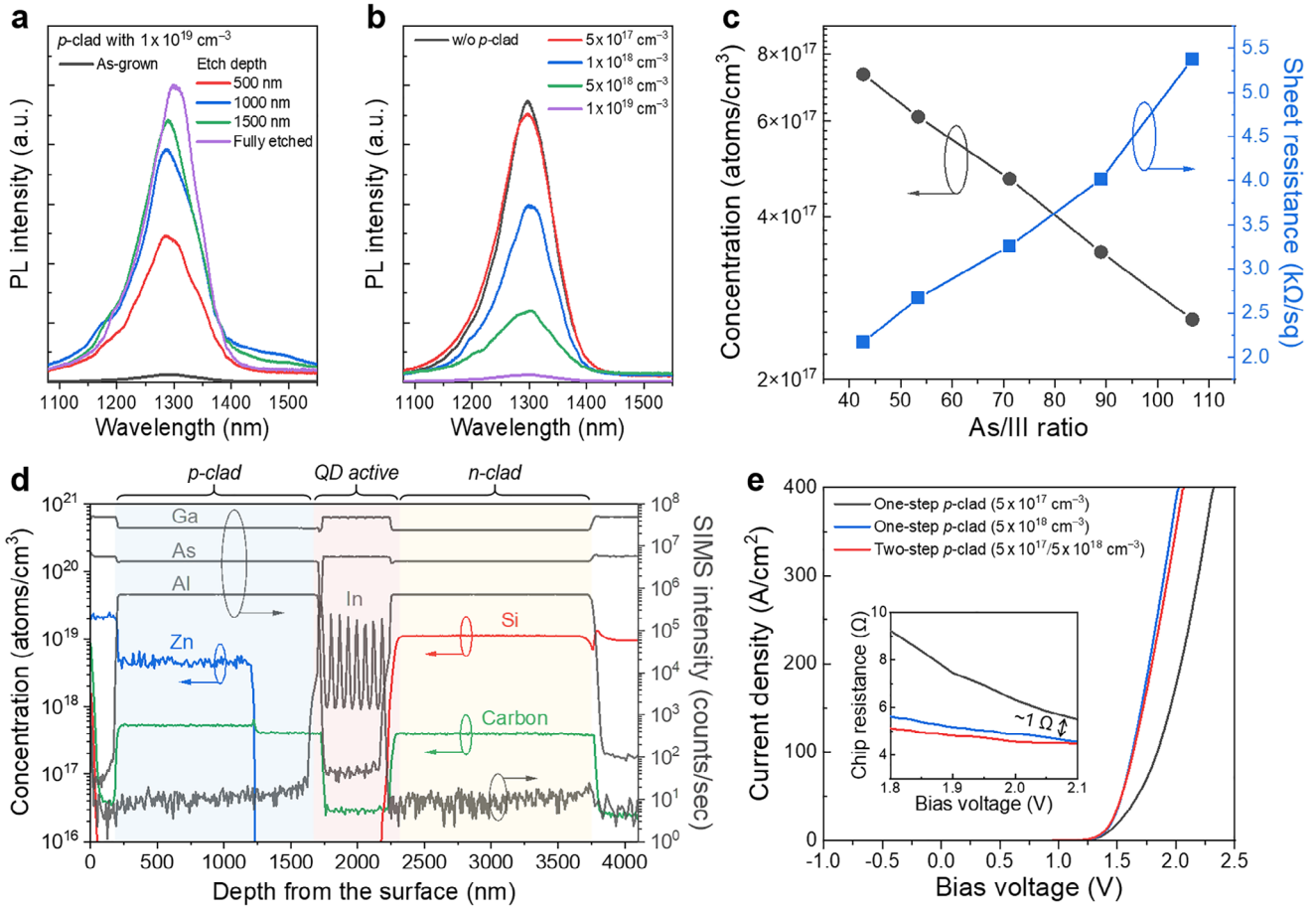

Figure 2. Low-temperature MOCVD growth of *p*-AlGaAs cladding layers and their material characteristics. a) PL spectra of the QDLDs with a heavily doped *p*-cladding layer depending on the etch depth. PL intensity increases as the etch depth is increased due to reduced free carrier absorption. b) PL spectra of the QDLDs with various doping concentrations in the *p*-cladding layer. PL spectra show almost identical results between samples without a *p*-cladding layer and with a *p*-cladding layer (5×10^{17} cm^{-3} doped). c) Hall measurement results of *p*-AlGaAs layer, showing carrier concentration and sheet resistance depending on the As/III ratio. d) ToF-SIMS depth profile of grown QDLD heterostructure with low-temperature two-step *p*-AlGaAs cladding layer. e) Measured *J*–*V* curves of the laser diodes with one-step *p*-cladding layer and two-step *p*-cladding layer. The two-step *p*-cladding layer is composed of a 1 μm-thick heavily doped *p*-AlGaAs layer and 0.5 μm-thick naturally *p*-doped AlGaAs layer.

the doping concentration of the unintentionally doped *p*-AlGaAs layer was examined by adjusting the V/III ratio without intentional Zn doping. Figure 2c shows that a V/III ratio of 70 is the optimized growth condition to achieve a 5×10^{17} cm^{-3} hole density. The doping level variation of the unintentionally doped *p*-AlGaAs layers was also investigated via Hall effect measurements. We achieved consistent *p*-doping levels below 5×10^{17} cm^{-3} level. While this approach ensures minimum free carrier absorption, the relatively low doping concentration can increase the device resistance. To avoid this issue, we therefore used a two-step *p*-AlGaAs clad structure.

Figure 2d shows the time-of-flight secondary ion mass spectrometry (ToF-SIMS) results of the grown QDLDs with the two-step *p*-AlGaAs clad structure. The left and right axes represent doping concentration and SIMS intensity, respectively, and the doping concentration was derived from the calibration of the SIMS results. The Zn, Si, and C were observed as the dopants in each *p*- and *n*-AlGaAs cladding and contact layers. The other elements in the InAs/GaAs QDLDs, such as gallium (Ga), Al, indium (In), and arsenide (As) were also detected in each layer. The Zn and C were used as a *p*-type dopant, and Si was used as an *n*-type dopant. Owing to the intrinsic characteristics of MOCVD system and the use of metal-organic sources, the C atoms, despite belonging to group IV, inevitably act as *p*-dopants in the AlGaAs layers. For the *p*-AlGaAs cladding layers, we used two-step growth, which is composed of 1 μm-thick Zn-doped AlGaAs layer and 500 nm-thick unintentionally C-doped AlGaAs layer. With our own strategy, we tried to solve the free-carrier absorption and the LD resistance increase.

Figure 2e depicts the current density–voltage (*J*–*V*) characteristics of QDLDs with one-step AlGaAs layers and two-step AlGaAs layers. The one-step AlGaAs layer with a doping concentration of 5×10^{17} cm^{-3} shows a higher resistance compared to the others. Meanwhile, the two-step *p*-AlGaAs layer and one-step *p*-AlGaAs with a doping concentration of 5×10^{18} cm^{-3} show a negligible difference. The inset of Figure 2e depicts the chip resistance as a function of bias voltage. A resistance difference of ≈1 Ω is measured between the one-step *p*-AlGaAs layer (with 5×10^{17} cm^{-3})

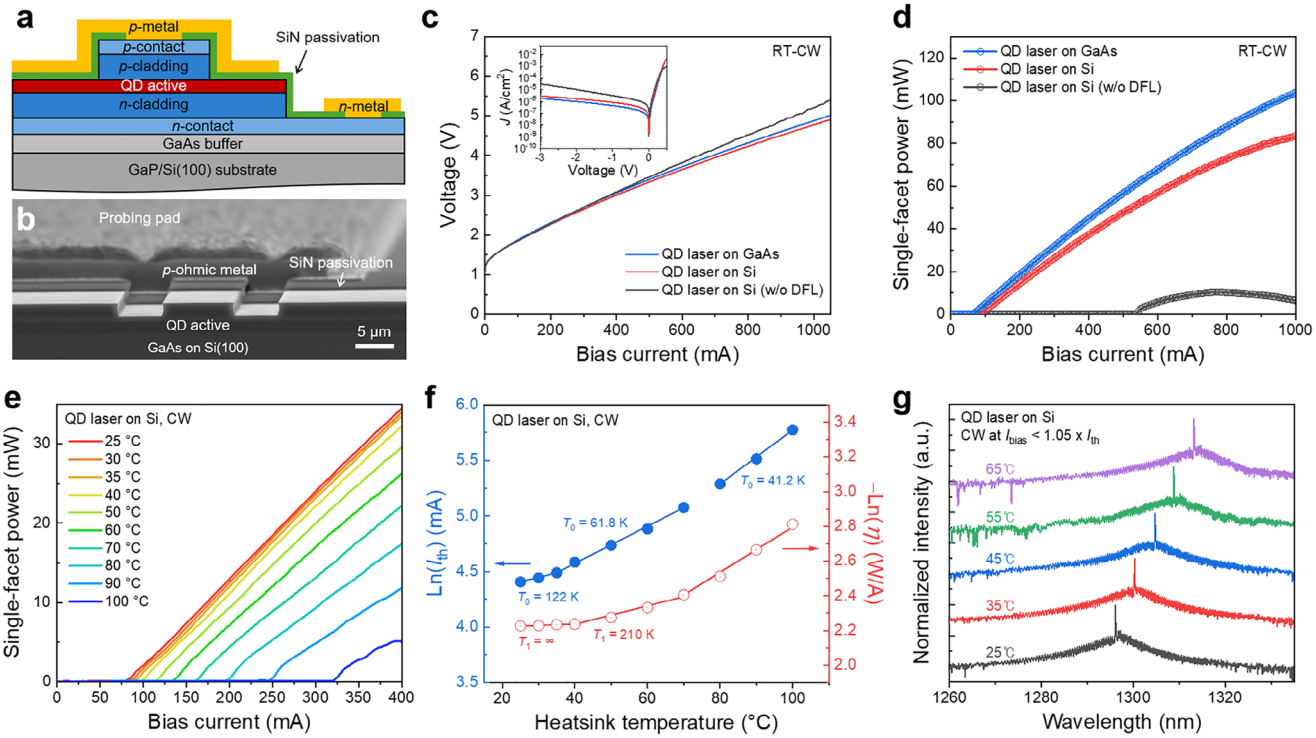

Figure 3. Lasing and temperature performance characteristics of the fabricated QDLDs. a) Schematic of the fabricated QDLD with a ridge-waveguide LD structure, utilized for performance verification of the grown InAs/GaAs QDs on Si. b) Cross-section SEM image of the fabricated QDLD, showing the clean cleaved facet for the Fabry–Pérot etalon mirror. c) *I–V* characteristics of the QDLDs on Si with and without the DFL, as well as the QDLD on native GaAs. All three LDs were fabricated using identical processes. LD width is 10 μm and cavity length is 2.5 mm. Inset, the measured current density as a function of the bias voltage, showing larger leakage current in the QDLD on Si without DFL, compared to the QDLD on Si (with DFL) and QDLD on GaAs. d) *L–I* characteristics of three different QDLDs measured under room-temperature CW operation. Lasing performance of the QDLD on Si with DFL is comparable to that of the QDLD on a native GaAs substrate. e) Temperature-dependent *L–I* curve of the QDLD on Si with DFLs, measured under CW operation. Maximum operation temperature for CW lasing is 100 °C. f) Threshold current and slope efficiency as a function of the heatsink temperature. The characteristic temperature T_0 (T_1) of the QDLD on Si is extracted to be 122 K (∞) between 25–40 °C and 61.8 K (210 K) between 40–70 °C, indicating that the lasing characteristics of the fabricated QDLD on Si are insensitive to temperature changes. g) Measured temperature-dependent CW lasing spectra of the fabricated QDLD on Si.

and a two-step *p*-AlGaAs layer at ≈2 V. Note that the free carrier absorption is generally the strongest near the interface between the active DWELL layer and *p*-AlGaAs cladding layer. For these reasons, our two-step *p*-AlGaAs cladding layer that consists of 1-μm high Zn-doped layer and 0.5-μm low C-doped layer is expected to minimize the free-carrier absorption while maintaining low diode resistance. In addition, the basic laser performance comparison of the QDLDs with varying *p*-clad doping concentrations was also performed using light–current measurements under room-temperature CW operation, and the results are summarized in Figure S1 (Supporting Information).

2.3. Laser Fabrication and Performance Characterizations

To verify the QDLD performance and its applicability as light sources for Si photonic applications, we fabricated ridge-waveguide LDs using standard photolithography and analyzed their lasing characteristics. The fabrication of the QDLD was conducted with a two-inch wafer scale as described in Figure S2 of Supporting Information. **Figure 3a** shows a schematic of the fabricated QDLD. The laser fabrication started with a 10 μm-wide ridge waveguide patterning using an inductively-coupled-plasma reactive-ion etching (ICP-RIE) system. Ti/Pt/Au and Pd/Ge/Au stacks were deposited for *p*-side and *n*-side metal contacts, respectively, after the surface passivation with a silicon nitride (Si_3N_4) film. The annealing process for ohmic contacts was conducted at 200 °C, which can suppress film stress and avoid thermal cracks during the device fabrication processes.[27] After the 3 μm-thick gold pad deposition for probing, the substrate was thinned down to ≈120 μm and cleaved into LD bars with varying cavity lengths from 1 to 4 mm. The cross-section scanning electron microscopy (SEM) image of the fabricated QDLD is shown in Figure 3b, confirming that a Fabry–Pérot etalon mirror is clearly formed on the cleaved facet. To observe the intrinsic characteristics of the QDLDs, no high-reflection (HR) or anti-reflection (AR) films were coated on both facets in this study. In addition, nominally identical QDLDs grown on a native GaAs substrate and a Si substrate without DFLs were also fabricated together with the QDLDs on Si with DFLs for performance comparisons.

Lasing performance of the fabricated QDLDs was characterized with light–current–voltage (*L–I–V*) measurements under CW operation. Figure 3c shows the *I–V* characteristics of the three different LD devices with a 2.5 mm cavity length in the

forward bias range. All three QDLDs show a similar turn-on voltage and LD resistance; however, the QDLD on Si without DFLs exhibited a notably increased leakage current as shown in the inset of Figure 3c due to the high TDDs.[28] Accordingly, the as-cleaved single-facet optical power (P_{out}) of the QDLD on Si (without DFLs) was limited to ≈10 mW due to the thermal rollover. The threshold current (I_{th}) was also high, over 500 mA, as shown in the *L–I* curve measured at room temperature (RT) (Figure 3d). In contrast, for the QDLD on Si with DFL, the I_{th} was significantly reduced to ≈77 mA (J_{th} = 309 A cm^{-2}), even close to that of the QDLD on GaAs (I_{th} = 65 mA, J_{th} = 260 A cm^{-2}). Additionally, the single-facet output power exceeded 80 mW under CW operation. That is, although both the QDLDs grown on Si show a similar turn-on voltage and LD resistance, the QDLD with DFLs exhibits excellent lasing performance, approaching that of the QDLDs grown on the native GaAs substrate. Moreover, the threshold current densities of the QDLD on Si with DFLs could be further lowered to an average of 255 A cm^{-2} in 4 mm LD bars (see Figure S3, Supporting Information), which is the record-low value for any MOCVD-grown QD lasers on Si and even comparable to the best performing devices grown by MBE.

In order to confirm whether the QDLD on Si can be utilized in a wide range of Si photonic applications, temperature-dependent *L–I* measurements were performed under CW operation, as shown in Figure 3e. Slight changes in I_{th} and slope efficiency (η) were observed up to 50 °C, and beyond this temperature, the lasing characteristics were degraded gradually. The maximum lasing temperature of the QDLD on Si with DFLs was 100 °C under CW operation and extended up to 115 °C under a 2% pulsed operation (see Figure S4, Supporting Information). It should be noted that the controllable temperature of our heatsink stage was limited to 115 °C, which indicates that the maximum lasing temperature under pulsed operation can be extended further beyond this temperature. The characteristic temperatures, T_0 and T_1 related to the thermal stability of LDs, were analyzed from the measured temperature-dependent *L–I* curves. The T_0 and T_1 were extracted by fitting the exponential functions of $I_{th} = I_0\exp(T/T_0)$ and $\eta = \eta_0\exp(-T/T_1)$, respectively, and the results are described in Figure 3f. The estimated T_0 of the QDLD on Si with DFLs was 122 K between 25 and 40 °C and 61.8 K between 40 and 70 °C. Meanwhile, the estimated T_1 ranged ∞ between 25 and 40 °C, and 210 K between 40 and 70 °C. The characteristic temperatures T_0 and T_1 under a pulsed mode were also described in Figure S4 (Supporting Information), showing higher T_0 and T_1 values than those obtained under CW operation. These thermally stable LD characteristics suggest that the QDLD on Si with DFLs can be utilized in photonic integrated circuits operating in high-temperature environments such as data centers. It should also be noted that the maximum lasing temperature and characteristic temperature values of the QDLD on Si with DFLs are comparable to those of the QDLD on native GaAs (see Figure S5, Supporting Information).

Figure 3g shows the temperature-dependent CW lasing spectra at an injection current near I_{th}. The center wavelength of the lasing peak of the QDLD on Si with DFLs was ≈1296 nm at 25 °C, which matches the center wavelength of the PL spectrum as depicted in Figure 1h. As the temperature increased, the center lasing wavelength was red-shifted by 0.42 nm °C^{-1}, while a ground-state CW lasing characteristic was maintained in the measurement temperature range. This wavelength red shift is nearly comparable to or slightly lower than those reported in previous studies.[12,14] In the case of the QDLD on GaAs, the center wavelength was red-shifted by 0.35 nm °C^{-1}. The slightly less red-shift in the QDLD on GaAs is possibly due to the lower I_{th} and consequently reduced local heating effects, in comparison to the QDLD on Si (as summarized in Figure S6, Supporting Information). It should be noted that a more accurate evaluation of temperature-dependent lasing spectra in QDLDs can be achieved through rigorous spectral measurements under pulsed-mode operation and/or using advanced techniques capable of directly probing the internal junction temperature. Such systematic analyses will be addressed in our follow-up studies.

2.4. QD Laser Reliability Characterizations

Achieving high reliability with a sufficient lifetime is critical for practical applications of our QDLDs grown on Si. We investigated extrapolated device lifetimes of the fabricated QDLDs on Si by evaluating mean-time-to-failure (MTTF): that is, time to double the initial value for I_{th} and a bias current required for 10 mW P_{out} (I_{10mW}). For this purpose, the QDLD on Si was aged over 2000 h at 55 °C, which is the operation temperature of semi-cooled lasers for optical communications,[29,30] under a constant DC current. *L–I–V* measurements were periodically performed at RT to monitor the aged lasing characteristics. The aging current was reset at $I = 1.75 \times I_{th}$ every time we swept *L–I–V*, which led to an increase in the aging currents from 150 to 220 mA. **Figure 4a** shows the evolution of the measured CW *L–I* curves during the 2000 h aging tests. The I_{th}, slope efficiency, and I_{10mW} were degraded relatively rapidly at the beginning, and then those were saturated gradually over the whole course of aging. These trends are summarized in Figure 4b. Negligible changes in I_{th} and I_{10mW} are observed after the aging period of 500 h. From the aging data, the MTTF (device lifetime) values were extracted through the linear fitting for I_{th} and I_{10mW} in the semi-log scale aging plots,[14] as shown in Figure 4c,d. Note that the coefficient of determination (R^2) is greater than 99.9%, which indicates the high fitting accuracy of this method. As a result, the extrapolated MTTF for I_{th} was estimated to be ≈497 years, while the estimated MTTF for I_{10mW} was even higher, ≈1050 years, which are remarkably long lifetimes considering the high aging temperature (55 °C). It should also be noted that these MTTF values extracted from the QDLD on Si are even comparable to those for the QDLDs on native GaAs, which is a more reliable platform to grow high-quality QDLDs (see Figure S7, Supporting Information). The result implies that the all-MOCVD-grown QDLDs on Si substrates have superior device reliability to those grown by MBE.

3. Discussion

Table 1 shows significant strides in the reliability improvements of the MBE-grown QDLDs on Si.[9,11,14,31,32] Industrial applications typically require 20 years of expected device lifetime, and only the recent QDLD on Si with dislocation trapping layers satisfied the requirement.[14] Our lasers do not contain such

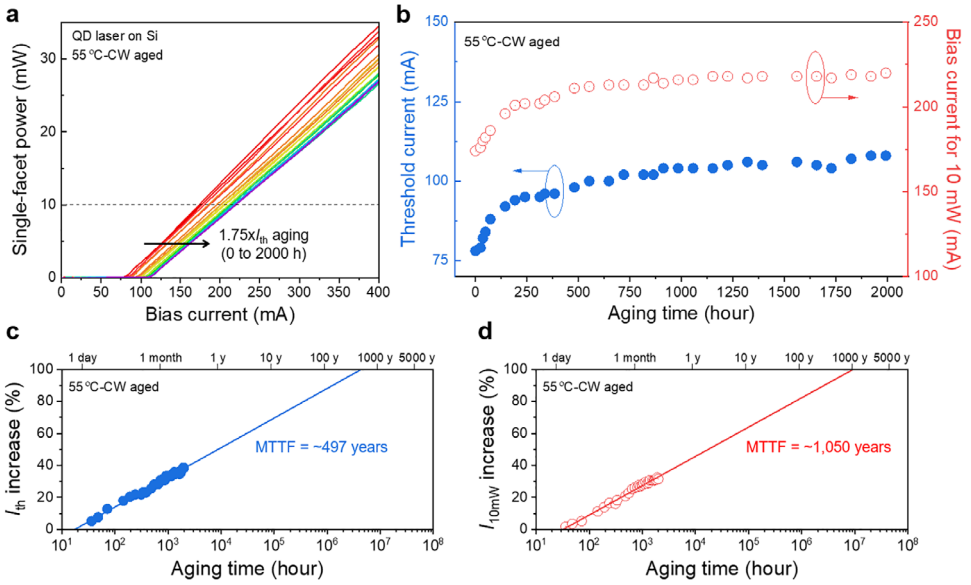

Figure 4. Laser lifetime characterizations for QDLD on Si. a) Evolution of the CW *L–I* characteristics of fabricated QDLD on Si during 2000 h aging at 55 °C. A DC current ranging from 150 mA to 220 mA (1.75 times the threshold current at 55 °C) was applied to device during aging test, and periodic CW *L–I–V* measurements were conducted for monitoring the aged lasing characteristics. b) Changes in threshold current and bias current required for 10 mW optical output power over aging time. c) Extraction of mean-time-to-failure (MTTF) for threshold current by linear fitting of the percent increase in threshold current against log-scale aging time. d) MTTF extraction of the bias current for 10 mW by using the identical fitting procedure. *R*-square values indicating the fitting accuracy are greater than 99.9%. The extrapolated MTTF of the threshold current is ≈497 years, and that of the bias current required for 10 mW output power is ≈1050 years.

Table 1. Summary of the device reliability for MBE-grown QDLDs on Si, and comparison with this work achieved by all MOCVD epitaxy.

Year	Epitaxy tool	TDD	Aging temperature	Aging current	MTTF	Reference
2015	MBE	≈10^8 cm^{-2}	30 °C	≈2000 A cm^{-2} (3×J_{th})	4 627 h	[31]
2016	MBE	≈10^5 cm^{-2}	26 °C	≈130 A cm^{-2} (1.75×J_{th})	100 158 h	[11]
2018	MBE	7 ×10^6 cm^{-2}	35 °C	≈500 A cm^{-2} (2×J_{th})	>20 years	[9]
2018	MBE	7 × 10^6 cm^{-2}	60 °C	≈1300 A cm^{-2} (2×J_{th})	65 000 h	[32]
2021	MBE	1.5 × 10^6 cm^{-2}	80 °C	≈1100 A cm^{-2} (2×J_{th})	>20 years	[14]
2024	**MOCVD**	**9 × 10^6 cm^{-2}**	**55 °C**	**600–800 A cm^{-2} (1.75×J_{th})**	**>20 years**	**This work**

trapping layers around the active region but showed much reliable results compared to the MBE-grown counterparts with similar TDD values. We believe that this could be due to the absence of innate oval defects in MOCVD growth.[33] MBE growth inevitably generates oval defects from solid source evaporations, and these can be sources of recombination-enhanced dislocation climbs.[31] Therefore, MOCVD growth is considered more advantageous than MBE for the growth of reliable QDLDs on Si. **Figure 5** summarizes the performances of InAs/GaAs QD lasers epitaxially grown on Si using MBE and/or MOCVD. Lasers integrated onto Si are desired to have low threshold current density to save power consumption and high lasing temperature to persist in harsh working environments. Our results demonstrated far superior performance compared to the other two all-MOCVD lasers. When compared to those grown by MBE, our QD lasers still show better performance regarding low threshold current and maximum lasing temperature.

4. Conclusion

In conclusion, we demonstrated high-performance InAs/GaAs QD lasers monolithically integrated on Si substrates using all MOCVD epitaxial growth. Highly uniform InAs QDs and their excellent crystalline quality were preserved by adopting a two-step *p*-AlGaAs cladding growth. Insertion of threading dislocation filter layers significantly improved the performance of our QD lasers on Si, including ultralow threshold current density and superior device reliability. Our demonstration suggests that monolithic integration of efficient, scalable, reliable III-V light sources onto Si photonic platforms has progressed beyond the research lab and is now poised for a commercially viable technology. The next step will be to implement our growth techniques onto Si waveguide-patterned substrates for light coupling, which can further lead to laser-integrated Si photonic integrated circuits with modulators, multiplexers, and photodetectors. Overall, we believe that this work represents a major milestone for

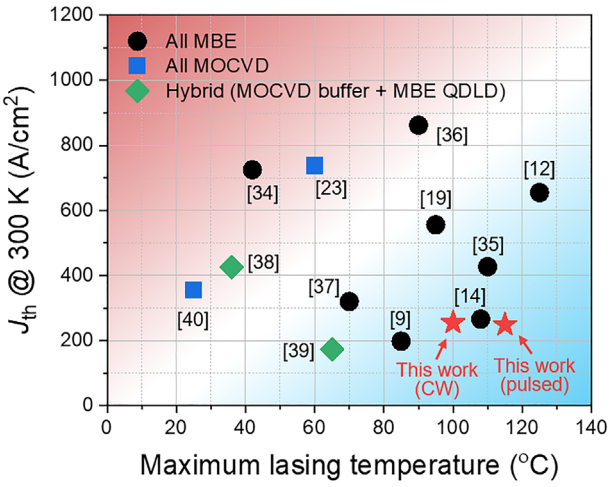

Figure 5. Performance benchmarks of III-V QD lasers epitaxially grown on Si using MBE and/or MOCVD. Continuous-wave threshold current densities at 300 K are plotted against the maximum lasing temperature. Detailed data sources are available in references.[9,12,14,19,23,34–40]

on-chip optical interconnect and Si-based photonic integrated circuits.

5. Experimental Section

Epitaxial Growth: The InAs/GaAs QDLD heterostructures were epitaxially grown on an on-axis GaP/Si (100) wafer by a vertical-type MOCVD reactor. The GaP/Si template, sourced from NAsP's commercially available product, included a 45 nm-thick GaP layer pseudomorphically grown on Si (100) by MOCVD to suppress anti-phase boundaries.[41] Prior to the GaAs growth, the GaP/Si templates were cleaned with diluted HF and annealed at 900 °C in an H_2/PH_3-rich atmosphere. Starting with the epitaxial growth of a low-temperature 20 nm GaAs layer at 420 °C, an additional GaAs layer with a 900 nm thickness was subsequently grown in two stages. This was followed by thermal cycling annealing (TCA) between 800 and 350 °C. After the TCA, three pairs of the $In_{0.14}Ga_{0.86}As$/GaAs DFL and 300 nm GaAs spacer layer were grown sequentially. Each DFL consisted of ten sets of a superlattice structure with alternating 10 nm-thick $In_{0.14}Ga_{0.86}As$ and GaAs layers, and the growth temperature was optimized based on the previous studies.[42] To compare the device performance, a control sample without DFLs, but with the same GaAs buffer thickness, was also grown. After the GaAs buffer growth with and without the DFLs, the quality of the GaAs buffer on Si was characterized by ECCI measurements to evaluate the TDD. Finally, the QDLD heterostructures, consisting of a 1.5 µm *n*-AlGaAs cladding layer, seven pairs of DWELL active layers, and a 1.5 µm *p*-AlGaAs cladding layer, were grown simultaneously on both the GaAs buffer on Si (with and without DFLs) and on native GaAs wafer.

Material Characterizations: The quality of the QDLD heterostructures was evaluated by TEM, SEM, ECCI, AFM, PL, Hall, and SIMS measurements. The cross-section images of the grown InAs/GaAs QDLD heterostructures were obtained by using field-emission TEM (Titan 80–300, FEI Inc.) and field-emission SEM (Phenom Pharos, Thermo Fisher Scientific Inc.) systems. The TDD levels within the GaAs buffer layers were assessed via the ECCI images from a TESCAN CLARA SEM system operated at an acceleration voltage of 30 keV. The density and uniformity of the grown InAs/GaAs QDs were characterized by AFM (NX20, Park Systems Inc.) with non-contact mode. The PL spectra of the QD heterostructures were measured by using a monochromator (SpectraPro-500i, Acton Research Corp.) and a PL mapper (MAPLE-II, Dong woo Optron Inc.) with a 980 nm excitation laser and a thermoelectrically cooled InGaAs detector, optimized for near-infrared emission collection. The carrier concentration and sheet resistance of the *p*-AlGaAs cladding layers were evaluated by van der Pauw-based Hall measurements (HL5500, Accent Inc.). The layer-by-layer depth profile of the as-grown QD heterostructure was obtained from ToF-SIMS measurements (CAMECA IMS 7*f* magnetic sector SIMS) with Cs^+ primary ions at a beam energy of 6 kV.

LD Fabrication: Following the epitaxial growth and material characterizations, ridge-waveguide QDLDs with 10-µm-wide stripes were fabricated by using standard photolithography and ICP-RIE processes. The as-grown QD epitaxial wafers were first cleaned with H_2SO_4 and diluted HF to remove native oxides, followed by the deposition of a 100 nm SiO_2 layer using a plasma-enhanced chemical deposition system (VL-LA-PECVD, Unaxis Inc.). Subsequently, a ridge waveguide with a 10 µm width was patterned by *i*-line stepper lithography (NSR2205i12D, Nikon Inc.) with a positive-tone photoresist (PR), and the ridge patterns were then transferred to the SiO_2 layer using a CF_4/O_2 plasma in a Plasma-Therm VLR RIE system. Using the transferred SiO_2 layer as a hard mask, the ridge waveguide was dry etched to a depth of 1.5 µm above the QD active layer through a Cl_2-based ICP-RIE system (Versaline LL-ICP, Plasma Therm Inc.). After surface passivation with a Si_3N_4 film and subsequent opening of the contact regions, the *p*-metal and *n*-metal were formed by using negative-tone PR patterning and lift-off processes. To form ohmic contacts with the p^+-GaAs and n^+-GaAs contact layers at a low annealing temperature of 200 °C, Ti/Pt/Au (300/500/2500 Å) and Pd/Ge/Au (150/450/2600 Å) metal stack was used for the anode and cathode. After the furnace annealing at 200 °C for 2 h, both the *p*- and *n*-metal contacts exhibited excellent ohmic behavior with a specific contact resistance below 3×10^{-6} Ω-cm^2. For heat dissipation and probing, 3 µm-thick Au pads were electroplated onto the *p*-metal and *n*-metal. Finally, the substrate was thinned down to ≈120 µm by using a lapping and polishing system (PM6, Logitech Inc.), and cleaved into long LD bars of the desired cavity length using a Daitron scribing/cleaving machine.

Device Characterizations: The electrical characteristics (diode *J–V* and leakage current) of the fabricated QDLDs were measured by using a semiconductor parameter analyzer (4156C, Agilent Inc.). Lasing performance and temperature characterizations were performed via the *L–I–V* measurements using an LD chipbar tester synchronized with a Keithley 2520 pulsed LD source meter, 2520INT-1-Ge pulsed power detector, and 2510-AT thermo-electric cooler. The CW lasing spectra were acquired with an optical spectrum analyzer (MS9740A, Anritsu Inc.). For the aging test, the fabricated QDLD chipbars were packaged onto an AlN/Cu submount and wire-bonded to metal pads pre-patterned on the submount. The packaged QDLD samples were then aged at 55 °C for 2000 h under a constant DC current, with the periodic *L–I–V* measurements to monitor the aged lasing characteristics.

Supporting Information

Supporting Information is available from the Wiley Online Library or from the author.

Acknowledgements

This work was supported by Electronics and Telecommunications Research Institute (ETRI) internal project (24RH1500, 24BH1400, and 23ZB1100), and Korea National Research Foundation (RS-2024-00437570).

Conflict of Interest

The authors declare no conflict of interest.

Data Availability Statement

The data that support the findings of this study are available from the corresponding author upon reasonable request.

Keywords

III-V lasers, epitaxial growth, MOCVD, QD/Si lasers, quantum dots (QDs)

Received: March 13, 2025
Revised: May 13, 2025
Published online:

[1] A. H. Atabaki, S. Moazeni, F. Pavanello, H. Gevorgyan, J. Notaros, L. Alloatti, M. T. Wade, C. Sun, S. A. Kruger, H. Meng, K. Al Qubaisi, I. Wang, B. Zhang, A. Khilo, C. V. Baiocco, M. A. Popović, V. M. Stojanović, R. J. Ram, *Nature* **2018**, *556*, 349.
[2] C. Sun, M. T. Wade, Y. Lee, J. S. Orcutt, L. Alloatti, M. S. Georgas, A. S. Waterman, J. M. Shainline, R. R. Avizienis, S. Lin, B. R. Moss, R. Kumar, F. Pavanello, A. H. Atabaki, H. M. Cook, A. J. Ou, J. C. Leu, Y.-H. Chen, K. Asanović, R. J. Ram, M. A. Popović, V. M. Stojanović, *Nature* **2015**, *528*, 534.
[3] D. Liang, J. E. Bowers, *Nat. Photonics* **2010**, *4*, 511.
[4] D. Liang, X. Huang, G. Kurczveil, M. Fiorentino, R. G. Beausoleil, *Nat. Photonics* **2016**, *10*, 719.
[5] Y. De Koninck, C. Caer, D. Yudistira, M. Baryshnikova, H. Sar, P.-Y. Hsieh, C. I. Özdemir, S. K. Patra, N. Kuznetsova, D. Colucci, A. Milenin, A. A. Yimam, G. Morthier, D. Van Thourhout, P. Verheyen, M. Pantouvaki, B. Kunert, J. Van Campenhout, *Nature* **2025**, *637*, 63.
[6] S. Shekhar, W. Bogaerts, L. Chrostowski, J. E. Bowers, M. Hochberg, R. Soref, B. J. Shastri, *Nat. Commun.* **2024**, *15*, 751.
[7] A. Rickman, *Nat. Photonics* **2014**, *8*, 579.
[8] Z. Yan, Y. Han, L. Lin, Y. Xue, C. Ma, W. K. Ng, K. S. Wong, K. M. Lau, *Light-Sci. Appl.* **2021**, *10*, 200.
[9] D. Jung, Z. Zhang, J. Norman, R. Herrick, M. J. Kennedy, P. Patel, K. Turnlund, C. Jan, Y. Wan, A. C. Gossard, J. E. Bowers, *ACS Photonics* **2018**, *5*, 1094.
[10] C. Shang, K. Feng, E. T. Hughes, A. Clark, M. Debnath, R. Koscica, G. Leake, J. Herman, D. Harame, P. Ludewig, Y. Wan, J. E. Bowers, *Light-Sci. Appl.* **2022**, *11*, 299.
[11] S. Chen, W. Li, J. Wu, Q. Jiang, M. Tang, S. Shutts, S. N. Elliott, A. Sobiesierski, A. J. Seeds, I. Ross, P. M. Smowton, H. Liu, *Nat. Photonics* **2016**, *10*, 307.
[12] Z. Lv, S. Wang, S. Wang, H. Chai, L. Meng, X. Yang, T. Yang, *Opt. Express* **2023**, *31*, 24173.
[13] J. Duan, H. Huang, B. Dong, D. Jung, J. C. Norman, J. E. Bowers, F. Grillot, *IEEE Photonics Technol. Lett.* **2019**, *31*, 345.
[14] C. Shang, E. Hughes, Y. Wan, M. Dumont, R. Koscica, J. Selvidge, R. Herrick, A. C. Gossard, K. Mukherjee, J. E. Bowers, *Optica* **2021**, *8*, 749.
[15] D. Jung, P. G. Callahan, B. Shin, K. Mukherjee, A. C. Gossard, J. E. Bowers, *J. Appl. Phys.* **2017**, *122*, 225703.
[16] Y. Wang, S. Chen, Y. Yu, L. Zhou, L. Liu, C. Yang, M. Liao, M. Tang, Z. Liu, J. Wu, W. Li, I. Ross, A. J. Seeds, H. Liu, S. Yu, *Optica* **2018**, *5*, 528.
[17] T. Zhou, M. Tang, G. Xiang, B. Xiang, S. Hark, M. Martin, T. Baron, S. Pan, J.-S. Park, Z. Liu, S. Chen, Z. Zhang, H. Liu, *Nat. Commun.* **2020**, *11*, 977.
[18] A. Remis, L. Monge-Bartolome, M. Paparella, A. Gilbert, G. Boissier, M. Grande, A. Blake, L. O'Faolain, L. Cerutti, J.-B. Rodriguez, E. Tournié, *Light-Sci. Appl.* **2023**, *12*, 150.
[19] W.-Q. Wei, A. He, B. Yang, Z.-H. Wang, J.-Z. Huang, D. Han, M. Ming, X. Guo, Y. Su, J.-J. Zhang, T. Wang, *Light-Sci. Appl.* **2023**, *12*, 84.
[20] B. Shi, B. Song, A. A. Taylor, S. S. Brunelli, J. Klamkin, *Appl. Phys. Lett.* **2021**, *118*, 122106.
[21] D. Guimard, M. Ishida, D. Bordel, L. Li, M. Nishioka, Y. Tanaka, M. Ekawa, H. Sudo, T. Yamamoto, H. Kondo, M. Sugawara, Y. Arakawa, *Nanotechnology* **2010**, *21*, 105604.
[22] S. M. Kim, Y. Wang, M. Keever, J. S. Harris, *IEEE Photonics Technol. Lett.* **2004**, *16*, 377.
[23] J. Wang, H. Hu, H. Yin, Y. Bai, J. Li, X. Wei, Y. Liu, Y. Huang, X. Ren, H. Liu, *Photonics Res.* **2018**, *6*, 321.
[24] D. M. Follstaedt, R. P. Schneider Jr., E. D. Jones, *MRS Online Proc. Libr.* **1993**, *326*, 61.
[25] L. Francesio, P. Franzosi, M. Caldironi, L. Vitali, M. Dellagiovanna, A. DiPaola, F. Vidimari, S. Pellegrino, *Il Nuovo Cimento D* **1996**, *18*, 975.
[26] H. Bracht, S. Brotzmann, *Phys. Rev. B* **2005**, *71*, 115216.
[27] L. C. Wang, P. H. Hao, J. Y. Cheng, F. Deng, S. S. Lau, *J. Appl. Phys.* **1996**, *79*, 4216.
[28] M. A. Mircovich, J. Kouvetakis, J. Menéndez, *J. Appl. Phys.* **2024**, *135*, 124501.
[29] N. D. Whitbread, A. J. Ward, B. de Largy, M. Q. Kearley, B. Asplin, P. J. Williams, M. J. Wale, *Proc. Eur. Conf. Opt. Commun.* **2008**, *3*, 177.
[30] T. Suzuki, H. Arimoto, T. Kitatani, A. Takei, T. Taniguchi, K. Shinoda, S. Tanaka, S. Tsuji, *Proceeding of the Optical Fiber Communication Conference*/National Fiber Optic Engineers Conference (OFC/NFOEC), Los Angeles, California United States March **2011**.
[31] A. Y. Liu, R. W. Herrick, O. Ueda, P. M. Petroff, A. C. Gossard, J. E. Bowers, *IEEE J. Sel. Top. Quantum Electron.* **2015**, *21*, 690.
[32] D. Jung, R. Herrick, J. Norman, K. Turnlund, C. Jan, K. Feng, A. C. Gossard, J. E. Bowers, *Appl. Phys. Lett.* **2018**, *112*, 153507.
[33] S. P. Tobin, S. M. Vernon, C. Bajgar, S. Wojtczuk, M. R. Melloch, A. Keshavarzi, T. B. Stellwag, S. Venkatensan, M. Lundstrom, K. A. Emery, *IEEE Trans. Electron Devices* **1990**, *37*, 469.
[34] T. Wang, H. Liu, A. Lee, F. Pozzi, A. Seeds, *Opt. Express* **2011**, *19*, 11381.
[35] A. Y. Liu, C. Zhang, J. Norman, A. Snyder, D. Lubyshev, J. M. Fastenau, A. W. K. Liu, A. C. Gossard, J. E. Bowers, *Appl. Phys. Lett.* **2014**, *104*, 041104.
[36] A. Y. Liu, J. Peters, X. Huang, D. Jung, J. Norman, M. L. Lee, A. C. Gossard, J. E. Bowers, *Opt. Express* **2017**, *42*, 338.
[37] J. Kwoen, B. Jang, J. Lee, T. Kageyama, K. Watanabe, Y. Arakawa, *Opt. Express* **2018**, *26*, 11568.
[38] S. Chen, M. Liao, M. Tang, J. Wu, M. Martin, T. Baron, A. Seeds, H. Liu, *Opt. Express* **2017**, *25*, 4632.
[39] Z. Liu, C. Hantschmann, M. Tang, Y. Lu, J.-S. Park, M. Liao, S. Pan, A. Sanchez, R. Beanland, M. Martin, T. Baron, S. Chen, A. Seeds, R. Penty, I. White, H. Liu, *J. Lightwave Technol.* **2020**, *38*, 240.
[40] P. Verrinder, L. Wang, B. Shi, S. Zhu, J. Klamkin, *Proceeding of the Conf. on Lasers and Electro-Optics (CLEO)*, San Jose, CA United States May **2023**.
[41] K. Li, J. Yang, Y. Lu, M. Tang, P. Jurczak, Z. Liu, X. Yu, J.-S. Park, H. Deng, H. Jia, M. Dang, A. M. Sanchez, R. Beanland, W. Li, X. Han, J.-C. Zhang, H. Wang, F. Liu, S. Chen, A. Seeds, P. Smowton, H. Liu, *Adv. Opt. Mater.* **2020**, *8*, 2000970.
[42] H. Kim, D.-M. Geum, Y.-H. Ko, W.-S. Han, *Nanoscale Res. Lett.* **2022**, *17*, 126.